Reverse-time migration using wavefield decomposition

Kittinat Taweesintananon

ABSTRACT

Reverse-time migration (RTM) is capable of imaging very steeply dipping reflectors and overhangs. However, it usually produces strong artifacts that contaminate the shallow parts of the migrated images. These artifacts can be suppressed using an imaging condition with appropriate decomposed source and receiver wavefields. In this paper, such a technique is applied and examined. This imaging condition keeps only energy at the points where strong backscattering originates. The results show that RTM using wavefield decomposition is a promising remedy for attenuating artifacts compared to the implementation of a low-cut filter. However, some artifacts still remain in the decomposed RTM image. These residual artifacts are caused by the cross-correlation between the upgoing component of the direct source wavefield and the backscattered component of the receiver wavefield.

INTRODUCTION

RTM is a migration method based on wavefield extrapolation in time. As a two-way wave-equation migration, it can image very steeply dipping reflectors and even overturned events. This method is based on two consecutive steps: numerical propagation of wavefields from the recording surface into image space, followed by the image formation process using these wavefields. RTM was first used for poststack depth migration of 2D seismic data in the late 1970s (Baysal et al., 1983; Whitmore, 1983).

Poststack RTM involves the extrapolation of receiver wavefields from recorded seismic data by computing the full two-way solution for the acoustic wave equation with time running backwards. In contrast, prestack RTM involves the extrapolation of source and receiver wavefields.

Prestack RTM for a shot profile consists of three steps: 1) forward extrapolating the source wavefield $S(t, \vec{x})$ from time $t = 0$ to $t = t_{\max}$, 2) backward extrapolating the receiver wavefield $R(t, \vec{x})$ from time $t = t_{\max}$ to $t = 0$, and 3) applying a suitable imaging condition to construct the reflectivity image (Biondi, 2005). The conventional imaging condition for RTM is the zero-lag cross-correlation of source and receiver wavefields (Claerbout, 1985). Since RTM is a type of shot-gather migration, each

shot profile is migrated independently. Thus, the final RTM image is the sum of the images from all individual profiles.

The extrapolated wavefields are full two-way solutions of the wave equation. These two-way solutions do not limit the propagation directions of wavefields. Therefore, RTM can correctly image very steeply dipping reflectors and even overturned events. In extremely complex areas, it can also handle strong lateral velocity variations and multi-path arrivals (Etgen et al., 2009). Thus, RTM can produce more accurate images than other popular migration methods such as Kirchhoff, beam, and one-way wave-equation migration. Nevertheless, the two major drawbacks of RTM are strong low-frequency artifacts and high computational cost. Such artifacts are generated due to the nature of the conventional RTM imaging condition. Many remedies, such as velocity smoothing and post-migration filtering, have been proposed to suppress these artifacts, but they all have severe limitations.

This paper focuses on a promising technique for attenuating artifacts in correlation-based RTM images called wavefield decomposition. This technique is to decompose source and receiver wavefields into the appropriate components based on their propagation direction, so that the decomposed wavefields can produce the image without artifacts (Liu et al., 2007, 2011). In this paper, I first provide an overview of RTM, its artifacts, and some common solutions for attenuating them. Next, I examine RTM using wavefield decomposition. Finally, I discuss the benefits and drawbacks of this technique and its practical implications.

REVERSE-TIME MIGRATION

For a single shot profile, the conventional correlation-based imaging condition for 2-D prestack RTM can be written as

$$I(\vec{x}) = \sum_{t=0}^{t_{\max}} S(t,\vec{x})R(t,\vec{x}), \tag{1}$$

where $t_{\max}$ is the maximum recorded time and $\vec{x} = (x, z)$ is the vector position of a wavefield in 2-D space. Source and receiver wavefields are extrapolated in time by solving the acoustic wave equation

$$\left(\frac{1}{v^2(\vec{x})}\frac{\partial^2}{\partial t^2} - \nabla^2\right) P(t,\vec{x}) = 0, \tag{2}$$

where $P(t,\vec{x})$ is the pressure wavefield, and $v(\vec{x})$ is the acoustic velocity in the computational domain.

In this paper, I use an explicit finite-difference method using a 2nd-order forward difference in time and a 4th-order central difference in space for wavefield extrapolation. The stability and antidispersion conditions for this method were described by Dablain (1986).

In practice, we can restrict the computational domain for wavefield extrapolation to only parts of the physical domain. Such a limitation produces artificial reflectors at the boundaries of the computational domain. In this study, I applied a Gaussian taper (Cerjan et al., 1985) along the artificial boundaries in order to suppress these undesired reflections. At the end of each Gaussian tapering region, I also applied an absorbing boundary condition using paraxial approximations of the acoustic wave equation (Clayton and Engquist, 1980). In this study, I applied absorbing conditions to all computational boundaries for extrapolating source and receiver wavefields, so that additional surface-related artifacts were suppressed.

To illustrate the wavefield extrapolation used, Figures 1(a) and 1(b) show an extrapolated wavefield in a constant-velocity model with a reflecting top boundary, whereas Figures 1(c) and 1(d) show an extrapolated wavefield in the same model with an absorbing top boundary instead. The extrapolation using such an absorbing top boundary was used to generate seismic data without surface-related multiples (SRM).

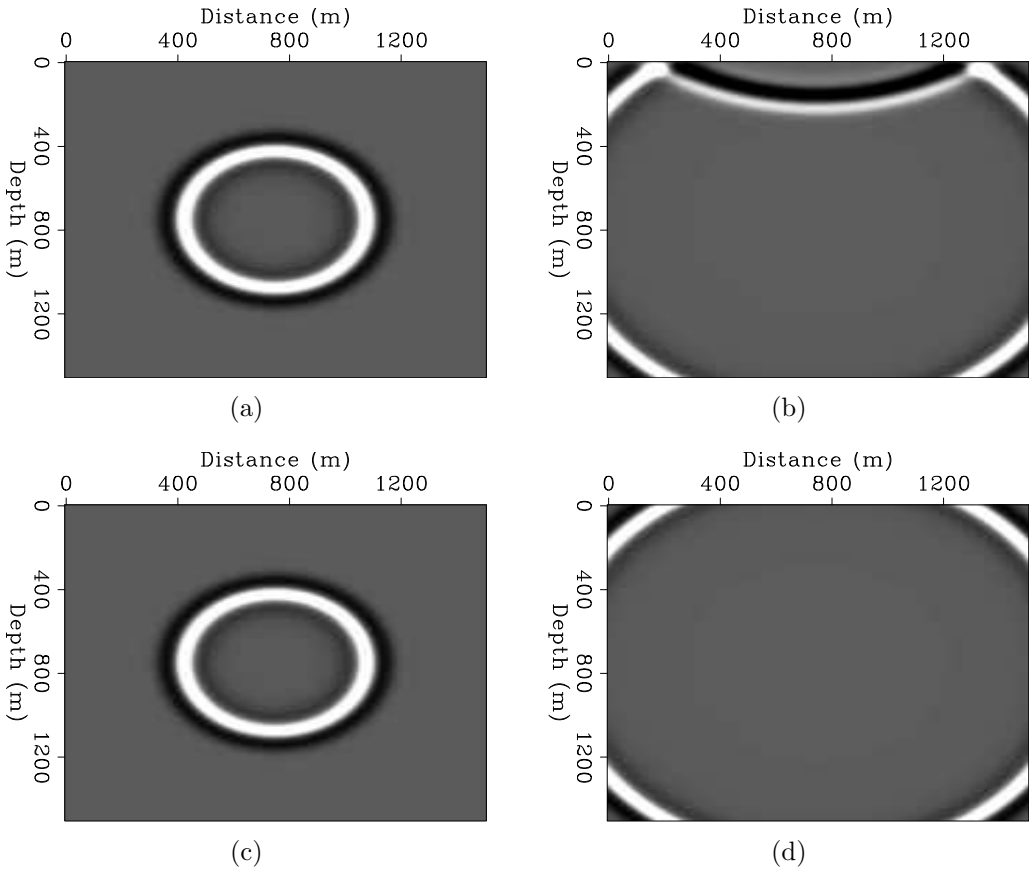

Figure 1: Wavefield snapshots illustrate the wavefield extrapolation used in this paper. (a) and (b) show snapshots from a single modeling experiment with a reflecting top boundary at 0.25 and 0.55 seconds, respectively. (c) and (d) show snapshots from a single modeling experiment with a nonreflecting top boundary at 0.25 and 0.55 seconds, respectively. [**ER**]

RTM ARTIFACTS AND REMEDIES

Strong RTM artifacts result from the undesired cross-correlations of head waves, diving waves, and backscattered waves (Yoon et al., 2004; Yoon and Marfurt, 2006). These artifacts are strong when high velocity contrasts are present, especially in the shallow regions. In addition, undesired artifacts caused by SRMs can also confuse the interpretation.

Figure 2(a) shows a simple 1-D velocity model consisting of a strong velocity contrast, whereas Figure 2(b) is a shot profile corresponding to this velocity model. Figure 3(a) shows the conventional RTM image from this shot profile using the true interval velocity as the migration velocity. The figure contains many artifacts due to head waves, diving waves, and backscattered waves at shallow depths. In addition, there are also artifacts due to SRMs at the bottom of the figure. Muting the head waves, diving waves, and direct waves before RTM can suppress the corresponding

artifacts as shown in Figure 3(b). In practice, the artifacts due to SRMs can be removed by using an appropriate SRM elimination program. Here, the synthetic data without SRM are generated by applying a nonflecting top boundary to wavefield extrapolation. Figure 4(b) shows the RTM image from the muted shot profile without SRM shown in Figure 4(a). Although artifacts due to head waves, diving waves, and SRM have been removed, the adverse effect of backscattered waves still remains above the strong reflector (Figure 4(b)). Thus, only RTM artifacts due to backscattered waves cannot easily be suppressed by pre-migration processing.

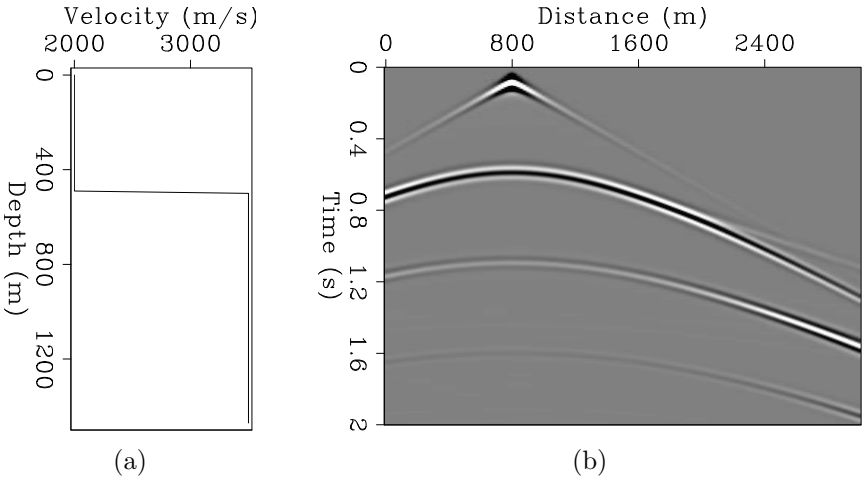

Figure 2: (a) 1-D true interval velocity model. (b) Synthetic shot profile from an explosive source on the surface in the velocity model (a). [**ER**]

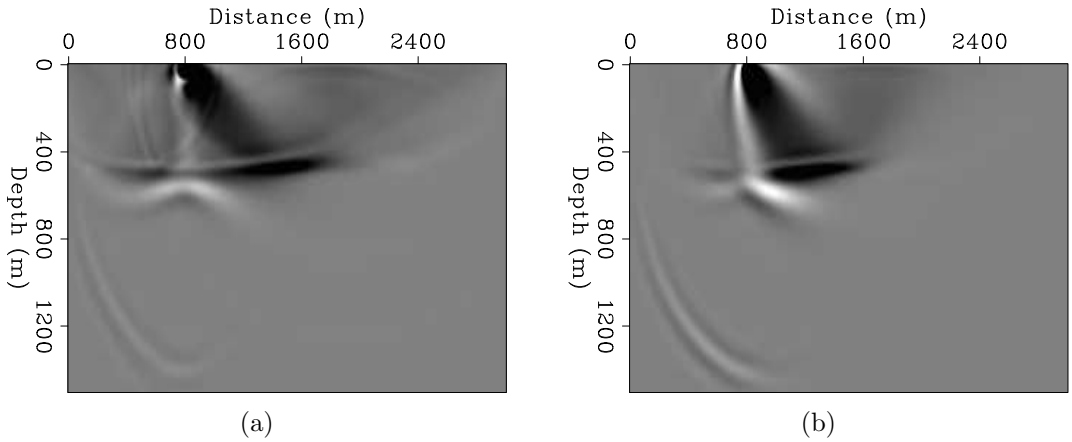

Figure 3: RTM images from the shot profile in Figure 2(b) before (a) and after (b) muting the head waves and diving waves. The true interval velocity shown in Figure 2(a) has been used as the migration velocity for both images. [**ER**]

Robein (2010) summarized four main approaches that have been used to suppress RTM artifacts due to backscattered waves: 1) smoothing the velocity model, 2) applying an appropriate filter to the post-migration image, 3) using nonreflecting wave propagation with directional damping, and 4) modifying the imaging condition.

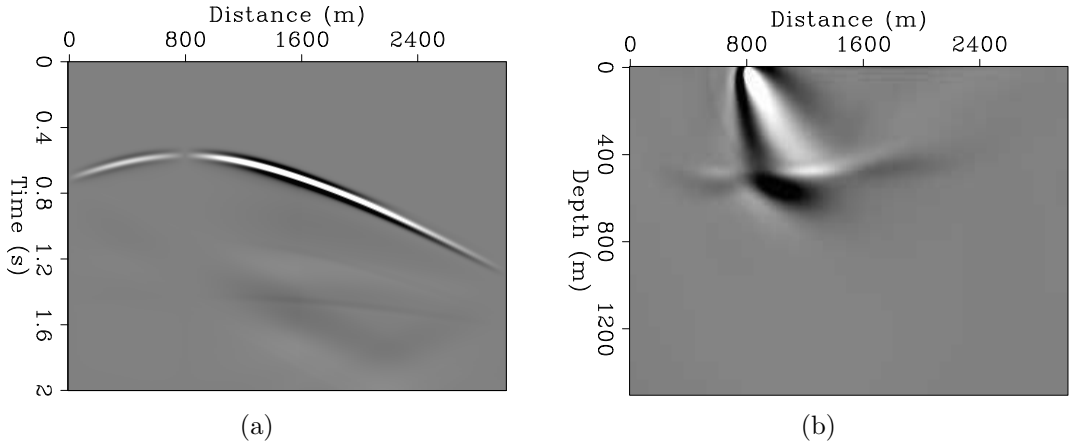

(a) (b)

Figure 4: (a) A shot profile without SRM after muting the head waves and diving waves; weighting and tapering are also applied. (b) An RTM image from this shot profile; the true interval velocity shown in Figure 2(a) has been used as the migration velocity. [**ER**]

Smoothing strong velocity contrasts can reduce the amplitude of undesired reflected waves; however, this can bias the accuracy of imaging due to incorrect velocity models. Figure 5(b) shows the same RTM image as Figure 4(b), but using the smoothed migration velocity shown in Figure 5(a). As shown in Figure 5(b), velocity smoothing can partly reduce the artifacts caused by backscattered waves; however, the artifacts still have an adverse effect on the shallow parts of the image. Although velocity smoothing can also cause other kinds of artifacts (Fei et al., 2010), this approach is currently used due to its robustness and low computational cost.

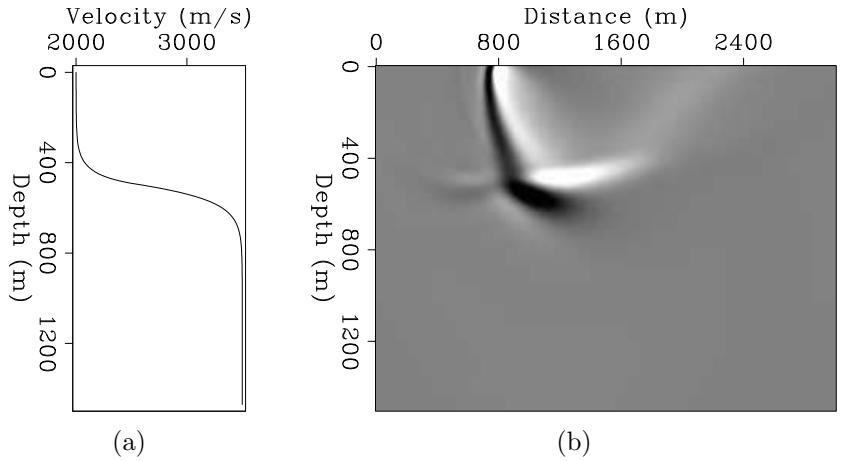

(a) (b)

Figure 5: The effects of velocity smoothing on the RTM image. (a) Smoothed migration velocity corresponding to the true interval velocity in Figure 2(a). (b) RTM image from muted data without SRM using this smoothed migration velocity (a). [**ER**]

There are many post-migration approaches whereby RTM artifacts are filtered after imaging. Low-cut filtering is an approach that can highly attenuate RTM artifacts as shown in Figure 6, where a causal low-cut filter was used. However, there still remains some noise in the figure. Moreover, low-cut filters can reduce the amplitude of steeply dipping reflectors, which mainly contain low-frequency information. Guitton et al. (2006) presented another possible post-migration solution by applying a least-squares filter to RTM images. In addition, the application of a Laplacian filter with appropriate pre- and post-migration processing is an effective solution that can remove RTM artifacts without hurting steeply dipping reflectors (Zhang and Sun, 2009).

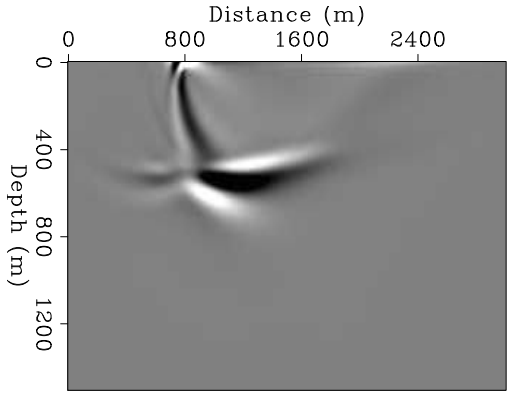

Figure 6: The RTM image in Figure 5(b) after applying a causal low-cut filter. [**ER**]

Applying a directional damping term to the wave equation can suppress unwanted internal reflections, including backscattered waves (Fletcher et al., 2006). This approach is more effective than velocity smoothing, since it does not alter the migration velocity. However, picking the problematic interfaces, which cause artifacts due to backscattered energy, is required in order to obtain directional damping coefficients. Therefore, the approach using directional damping is time consuming.

Modifying the imaging condition in RTM is another solution. This generally provides more effective noise attenuation than the other methods discussed above. The ultimate goal of this approach is to keep only energy along reflectors in the final image. There are various techniques used for modifying the imaging condition. The results of using different imaging conditions were discussed by Valenciano and Biondi (2003), Yoon et al. (2004), Liu et al. (2007), and Chattopadhyay and McMechan (2008).

RTM using wavefield decomposition is a method based on the modification of the imaging condition. This method modifies the imaging condition using wavefield decomposition in the Fourier domain, and was first introduced by Liu et al. (2007). This technique solves the problem of artifacts by suppressing their formation in the RTM algorithm. To demonstrate why this technique is worth investigation, we first need to understand the origin of RTM artifacts.

Origin of RTM artifacts due to backscattered waves

In order to investigate the origin of RTM artifacts due to backscattered waves, let us assume a flat interface with high velocity contrast as shown in Figure 7. The source wavefield (solid) and receiver wavefield (dashed) are extrapolated using a full propagator corresponding to Equation 2. When the propagated wavefields encounter this strong interface, part of the energy is transmitted and carries on downwards, while the remaining energy is reflected back to the surface. This phenomenon is observable for both source and receiver wavefields. Thus, at any point above the reflector, the corresponding source and receiver wavefields have exactly the same propagation paths, along which non-zero cross-correlations are produced (Robein, 2010; Liu et al., 2011). Accordingly, the cross-correlation of these wavefields creates not only the reflectivity image but also noise at all nonreflecting points along the propagation paths, such as point B and point C in Figure 7. Thus, low-frequency noise is a common characteristic of the RTM image with a strong reflector.

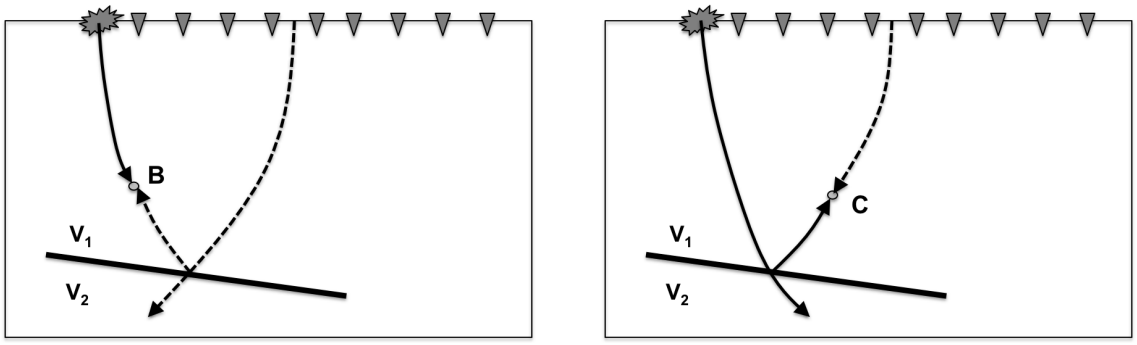

(a) (b)

Figure 7: The solid lines represent the propagation paths of a source wavefield, where the arrows indicate the propagation direction with time running forward. The dashed lines represent the propagation paths of a receiver wavefield, where the arrows indicate the propagation direction with time running backwards. [**NR**]

Note that, in this paper, I use the terms with the suffix *-going* such as *upgoing* and *downgoing* for describing the propagation direction of wavefields with time running **forward**. At point B in Figure 7(a), the downgoing source wavefield coincides in time with the propagated receiver wavefield that has been reflected. This receiver wavefield is indeed propagating downward with time running forward, i.e. downgoing receiver wavefield. On the other hand, at point C in Figure 7(b), the upgoing reflected source wavefield coincides in time with the upgoing receiver wavefield.

At either point B or point C in Figure 7, both source and receiver wavefields are propagating in the same direction and the same path with time running forward. Thus, the correlation-based images at point B and point C are caused by forward scattering events. These images are undesirable and can be considered to be noise, because they do not represent a reflected event. In contrast, at any point on the

reflector, source and receiver wavefields are propagating in opposite directions with respect to the normal vector of the reflector. Thus, the cross-correlation of these source and receiver wavefields, which results from backward scattering events, produces the desired image.

To keep only energy corresponding to backward scattering events in the final image, we might apply the cross-correlation to only the source and receiver wavefields that are propagating in opposite directions with respect to the reflector normal. This approach requires us to compute the propagation direction of both the source and receiver wavefields at every point in the computational domain. Although this approach involves intensive computation, it can provide the reflectivity images without forward scattering noise.

The computation of the wavefield propagation direction at every point in the compuational domain can be done using a Poynting vector (Yoon et al., 2004). This works well for simple models, but it does not produce satisfactory results in complex subsurface structures (Guitton et al., 2006). Xie and Wu (2006) applied the local one-way propagator, which is endowed with the Rayleigh integral, in order to decompose the wavefields. Another practical method is to decompose the wavefields in the Fourier domain in order to obtain the appropriate directional components of the wavefields based on Cartesian directions (Liu et al., 2007). This method is robust and worth investigation.

Wavefield decomposition based on Cartesian propagation directions can be used to modify the RTM imaging condition. This application was introduced by Liu et al. (2007, 2011), Suh and Cai (2009), and Fei et al. (2010). They all introduced methods to decompose source and receiver wavefields into one-way components along horizontal directions (leftgoing/rightgoing) and vertical directions (upgoing/downgoing). They then applied the zero-lag cross-correlation as the imaging condition to the appropriate combinations of these wavefield components. The results showed that such a method can effectively eliminate unwanted artifacts from conventional RTM images, and image quality was also improved.

Liu et al. (2007) applied wavefield decomposition in the F-K domain and obtained promising RTM results. The same authors later showed that a cheaper wavefield decomposition method in the wavenumber domain (T-K domain) can also provide the same results (Liu et al., 2011). Moreover, Suh and Cai (2009) applied a fan filter in the T-K domain before decomposing the filtered wavefields in the F-K domain. This approach produces better RTM images, but the computational cost significantly increases. In addition, Fei et al. (2010) illustrated how the decomposition method attenuates the artifacts in RTM images. However, Fei et al. (2010) did not provide the detail of the method they used to decompose the wavefields.

As mentioned above, Liu et al. (2007, 2011) advocated using wavefield decomposition for RTM in the Fourier domain. Next section, I describe this method with both horizontal and vertical propagation decompositions.

RTM USING WAVEFIELD DECOMPOSITION

A common method of wavefield decomposition is to obtain wavefields' one-way components with respect to two orthogonal directions, i.e. horizontal directions (leftgoing/rightgoing) and vertical directions (upgoing/downgoing). Hereafter I use the notations $z+$ to represent the downgoing wave component with respect to the vertical depth axis, and $x+$ to represent the rightgoing wave component with respect to the horizontal space axis. Note that a *downgoing* wavefield indicates a wavefield where the vertical direction of propagation is downward with time running forward, whereas a *rightgoing* wavefield indicates a wavefield where the horizontal direction of propagation is rightward with time running forward.

Source and receiver wavefields can be decomposed into their downgoing and upgoing components as follows (Liu et al., 2007):

$$S(t,\vec{x}) = S_{z+}(t,\vec{x}) + S_{z-}(t,\vec{x}), \tag{3}$$

$$R(t,\vec{x}) = R_{z+}(t,\vec{x}) + R_{z-}(t,\vec{x}), \tag{4}$$

where $S_{z+}(t,\vec{x})$, $S_{z-}(t,\vec{x})$, $R_{z+}(t,\vec{x})$ and $R_{z-}(t,\vec{x})$ are the downgoing and upgoing source and receiver wavefields, respectively. Similarly, they can also be decomposed into their horizontal components as follows:

$$S(t,\vec{x}) = S_{x+}(t,\vec{x}) + S_{x-}(t,\vec{x}), \tag{5}$$

$$R(t,\vec{x}) = R_{x+}(t,\vec{x}) + R_{x-}(t,\vec{x}), \tag{6}$$

where $S_{x+}(t,\vec{x})$, $S_{x-}(t,\vec{x})$, $R_{x+}(t,\vec{x})$ and $R_{x-}(t,\vec{x})$ are the rightgoing and leftgoing source and receiver wavefields respectively.

Thus, the conventional imaging condition can be separated into four imaging conditions based on combinations of vertical wavefield components:

$$\begin{aligned} I(\vec{x}) &= \sum_{t=0}^{t_{\max}} S_{z+}(t,\vec{x})R_{z-}(t,\vec{x}) + \sum_{t=0}^{t_{\max}} S_{z-}(t,\vec{x})R_{z+}(t,\vec{x}) \\ &\quad + \sum_{t=0}^{t_{\max}} S_{z+}(t,\vec{x})R_{z+}(t,\vec{x}) + \sum_{t=0}^{t_{\max}} S_{z-}(t,\vec{x})R_{z-}(t,\vec{x}) \\ &= I_{z,+-}(\vec{x}) + I_{z,-+}(\vec{x}) + I_{z,++}(\vec{x}) + I_{z,--}(\vec{x}). \end{aligned} \tag{7}$$

The first term is the cross-correlation of the downgoing source and upgoing receiver wavefields, which is equivalent to the result of downward continuing migration. The second term is the cross-correlation of the upgoing source and downgoing receiver wavefields. Thus, the first two terms can represent any reflector that causes vertical backscattering. The images corresponding to these two terms are caused by backward-scattered events with respect to the vertical axis. The subimages from the remaining two terms can be considered as noise, which results from vertical forward-scattered

events where source and receiver wavefields are vertically propagating in the same direction. Thus, the last two terms contribute to artifacts in RTM. However, these are related to tomographic information in wave-equation migration velocity analysis (Almomin et al., 2011).

In order to suppress RTM artifacts, the imaging condition that contains only the first two terms in Equation 7 (Liu et al., 2007, 2011) as

$$I_{\text{vert}}(\vec{x}) = \sum_{t=0}^{t_{\max}} S_{z+}(t,\vec{x})R_{z-}(t,\vec{x}) + \sum_{t=0}^{t_{\max}} S_{z-}(t,\vec{x})R_{z+}(t,\vec{x}). \tag{8}$$

This condition might be called the *vertical backscatter-based imaging condition*.

The *horizontal backscatter-based imaging condition* can be derived in a similar way. This horizontal imaging condition contains only cross-correlation of the source and receiver wavefields that are propagating in horizontally opposite directions:

$$I_{\text{horiz}}(\vec{x}) = \sum_{t=0}^{t_{\max}} S_{x+}(t,\vec{x})R_{x-}(t,\vec{x}) + \sum_{t=0}^{t_{\max}} S_{x-}(t,\vec{x})R_{x+}(t,\vec{x}). \tag{9}$$

The first term is the cross-correlation of the rightgoing source and leftgoing receiver wavefields. The second term is the cross-correlation of the leftgoing source and rightgoing receiver wavefields. Thus, this imaging condition represents any reflector that causes horizontal backscattering.

To use the benefits of both vertical and horizontal backscatter-based imaging conditions, they are added togather (Liu et al., 2011):

$$I(\vec{x}) = I_{\text{vert}}(\vec{x}) + I_{\text{horiz}}(\vec{x}). \tag{10}$$

This imaging condition might be called the *Cartesian backscatter-based imaging condition*. Note that the subimages from both vertical and horizontal imaging condition partly overlap, because of the overlap between the vertical and horizontal wavefield components. For example, the wavefield that is moving in any downright direction can be considered to be either downgoing or rightgoing.

In addition, the Cartesian backscatter-based imaging condition described above only involves the decomposition of source and receiver wavefields into their vertical or horizontal components. Thus, some backward-scattered events are indistinguishable from forward-scattered events using only this decomposition scheme. Therefore, the image illumination is reduced. However, Equation 10 produces no forward-scattered artifacts based on Cartesian directions of propagation. Thus, this proposed imaging condition can suppress artifacts in RTM images.

WAVEFIELD DECOMPOSITION

The conventional method for wavefield decomposition operates in the Fourier domain. This method was first applied to vertical seismic profiles (Hu and McMechan, 1987). Here, wavefields are decomposed into their upgoing and downgoing components in the F-K domain by using a 2-D fast Fourier transform (FFT):

$$\tilde{P}_{z+}(f,k_z) = \begin{cases} \tilde{P}(f,k_z) & \text{for } fk_z \geq 0 \\ 0 & \text{for } fk_z < 0 \end{cases}, \tag{11}$$

$$\tilde{P}_{z-}(f,k_z) = \begin{cases} 0 & \text{for } fk_z \geq 0 \\ \tilde{P}(f,k_z) & \text{for } fk_z < 0 \end{cases}, \tag{12}$$

where $\tilde{P}(f,k_z)$ is the 2-D Fourier transform of the wavefield $P(t,z)$ at any horizontal position x, and f and k_z are the frequency and vertical wavenumber representations of the wavefield. Note that the wavefield $P(t,z)$ can be either the source wavefield $S(t,z)$ or the receiver wavefield $R(t,z)$.

A similar method can be used to obtain the leftgoing and rightgoing components of wavefields:

$$\tilde{P}_{x+}(f,k_x) = \begin{cases} \tilde{P}(f,k_x) & \text{for } fk_x \geq 0 \\ 0 & \text{for } fk_x < 0 \end{cases}, \tag{13}$$

$$\tilde{P}_{x-}(f,k_x) = \begin{cases} 0 & \text{for } fk_x \geq 0 \\ \tilde{P}(f,k_x) & \text{for } fk_x < 0 \end{cases}, \tag{14}$$

where $\tilde{P}(f,k_x)$ is the 2-D Fourier transform of the wavefield $P(t,x)$ at any depth z, and f and k_x are the frequency and horizontal wavenumber representations of the wavefield.

In this paper, I apply smooth-cut F-K filters to the wavefield decomposition instead of using the sharp-cut filters shown in Equations 3 to 6, so that noise due to the FFT of discontinuous functions is reduced. Using smooth-cut filters might slightly reduce the illumination of reflectivity images, but it is worth attentuating the noise from FFT.

The decomposed wavefields, as in Equations 3 to 6, are the the 2-D inverse Fourier transforms of the decomposed wavefields derived from Equations 11 to 14. Thus, the terms on the right-hand sides of Equations 3 to 6 are all complex. However, in each equation, the summation of the imaginary parts becomes zero, and the wavefield is equal to the summation of the real parts of the decomposed wavefields; for example,

$$S(t,\vec{x}) = S_{z+}(t,\vec{x}) + S_{z-}(t,\vec{x}), \tag{15}$$

$$= \text{Re}[S_{z+}(t,\vec{x})] + \text{Re}[S_{z-}(t,\vec{x})]. \tag{16}$$

In their proposed imaging condition, Liu et al. (2007) applied only the real parts of the decomposed source and receiver wavefields to the imaging conditions in Equations 8 and 9. Thus, a question is raised about the effect that the imaginary components might have on the decomposed RTM images. Considering decomposed wavefields as complex functions, I rewrite Equations 8 and 9 to be

$$I_{\text{vert}}(\vec{x}) = \sum_{t=0}^{t_{\max}} S^*_{z+}(t,\vec{x}) R_{z-}(t,\vec{x}) + \sum_{t=0}^{t_{\max}} S^*_{z-}(t,\vec{x}) R_{z+}(t,\vec{x}), \tag{17}$$

and

$$I_{\text{horiz}}(\vec{x}) = \sum_{t=0}^{t_{\max}} S^*_{x+}(t,\vec{x}) R_{x-}(t,\vec{x}) + \sum_{t=0}^{t_{\max}} S^*_{x-}(t,\vec{x}) R_{x+}(t,\vec{x}), \tag{18}$$

where an asterisk denotes the complex conjugate. Equations 17 and 18 can be computed using only the wavefield decomposition in the T-K domain (Liu et al., 2011). Thus, this method is practical, because there is no need to save wavefields at every time step.

RESULTS AND DISCUSSION

I applied RTM using the imaging conditions proposed in the previous section to a single shot profile corresponding to the 1-D velocity model in Figure 2(a). The same approach was also applied to a synthetic data set derived from a 2-D velocity model windowed from the SEAM model. Because of its complicated structures, this synthetic data can illustrate the effectiveness of the proposed imaging conditions.

I found that the imaging condition that uses only the real parts of the decomposed wavefields (Equations 8 and 9) can produce the same images as the imaging condition that utilizes the complex-valued decomposed wavefields (Equations 17 and 18). Indeed, the difference between the RTM images derived from these two imaging conditions can be seen; however, the difference is negligible with respect to the RTM image. Thus, the imaginary parts have a negligible effect on the decomposed RTM image. Therefore, the imaging condition using only real parts of decomposed wavefields as in Equations 8 and 9 can replace the imaging conditions in Equation 17 and 18.

Examples with 1-D model

Figures 8(a) to 8(d) illustrate the vertically decomposed RTM images from a single shot profile without SRM corresponding to the model in Figure 2(a). These decomposed images are related to the four terms on the right-hand side of Equation 7. Figure 8(b) results from the upgoing source and downgoing receiver wavefields. This figure was expected to contain less artifacts; however, there are many artifacts above the reflector, as shown in Figure 8(b). I found that these artifacts in Figure 8(b)

were caused by cross-correlation between the upgoing component of the direct source wavefield and the downgoing component of the backscattered receiver wavefield. The upgoing component of the source wavefield that produces severe artifacts indeed propagates in almost horizontal directions, where it is indistinguishable from the downgoing source wavefield.

Figure 8(e) illustrates the RTM image corresponding to Equation 8, i.e. the vertical backscatter-based imaging condition. As shown in the figure, the horizontal reflector has been imaged well. However, there are artifacts at shallow depths resulting from those in Figure 8(b).

On the other hand, Figures 9(a) to 9(d) show the four horizontally different decomposed RTM images from a single shot profile without SRM corresponding to the model in Figure 2(a). Figure 9(e) illustrates the RTM image using the horizontal backscatter-based imaging condition as in Equation 9. The figure shows strong artifacts aligned vertically above the reflector. These artifacts have a similar origin as those in Figure 8(b), i.e. cross-correlation between the downgoing direct source wavefield and the backscattered receiver wavefield. Specifically, the component of the source wavefield that cause severe artifacts indeed propagates in almost vertical directions, where the leftgoing and rightgoing components of the source wavefield overlap.

Figure 10 illustrates the sum of the vertical and horizontal backscatter-based imaging conditions (Equations 10), i.e. the Cartesian backscatter-based imaging condition. As shown in the figure, the RTM artifacts at shallow depths have been attenuated except for the vertically aligned artifacts. These severe artifacts result from the cross-correlation between direct source wavefields and backscattered receiver wavefields. It can be seen that the RTM image using wavefield decomposition as in Figure 10 contains less artifacts compared to the conventional RTM image as in Figure 5(b). However, there is no significant improvement when comparing Figure 10 to the image after applying a low-cut filter (Figure 6).

Examples with complex 2-D model

Figure 11(a) shows a complex 2-D velocity model windowed from the SEAM model. This model is used for modeling a 2-D synthetic data set, which contains 69 shot profiles. This data set involves the deployment of a 1-D array of regularly spaced geophones (every 20 meters) on the entire surface. For each shot record, a source is exploded on the surface with 80-meter shot spacing. In the pre-migration process, muting head waves and diving waves is appied to this data set. However, SRM elimination is not implemented. For RTM, the smoothed velocity in Figure 11(b) is used.

Figure 12(a) illustrates a conventional RTM image using the cross-correlation imaging condition in Equation 1, whereas Figure 12(b) shows the same image after applying a causal low-cut filter. We can see that RTM artifacts are partially

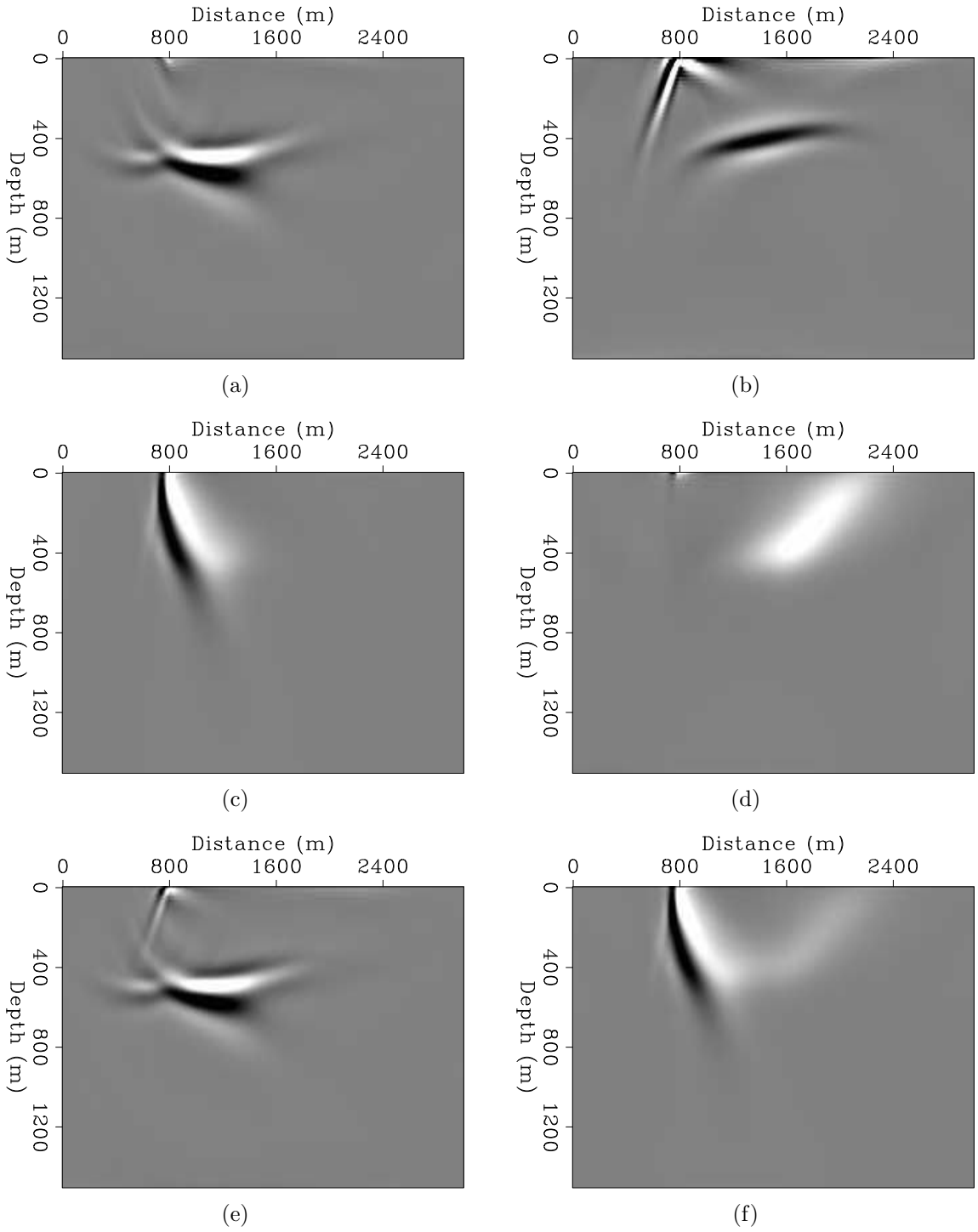

Figure 8: Different vertically decomposed RTM images from the single shot profile in Figure 4(a) along with smooth migration velocity in Figure 5(a): (a) using the downgoing source and upgoing receiver wavefields, (b) using the upgoing source and downgoing receiver wavefields, (c) using the downgoing source and downgoing receiver wavefields, and (d) using the upgoing source and upgoing receiver wavefields. (e) The sum of the images (a) and (b) equivalent to Equation 8. (f) The sum of the images (c) and (d). [**ER**]

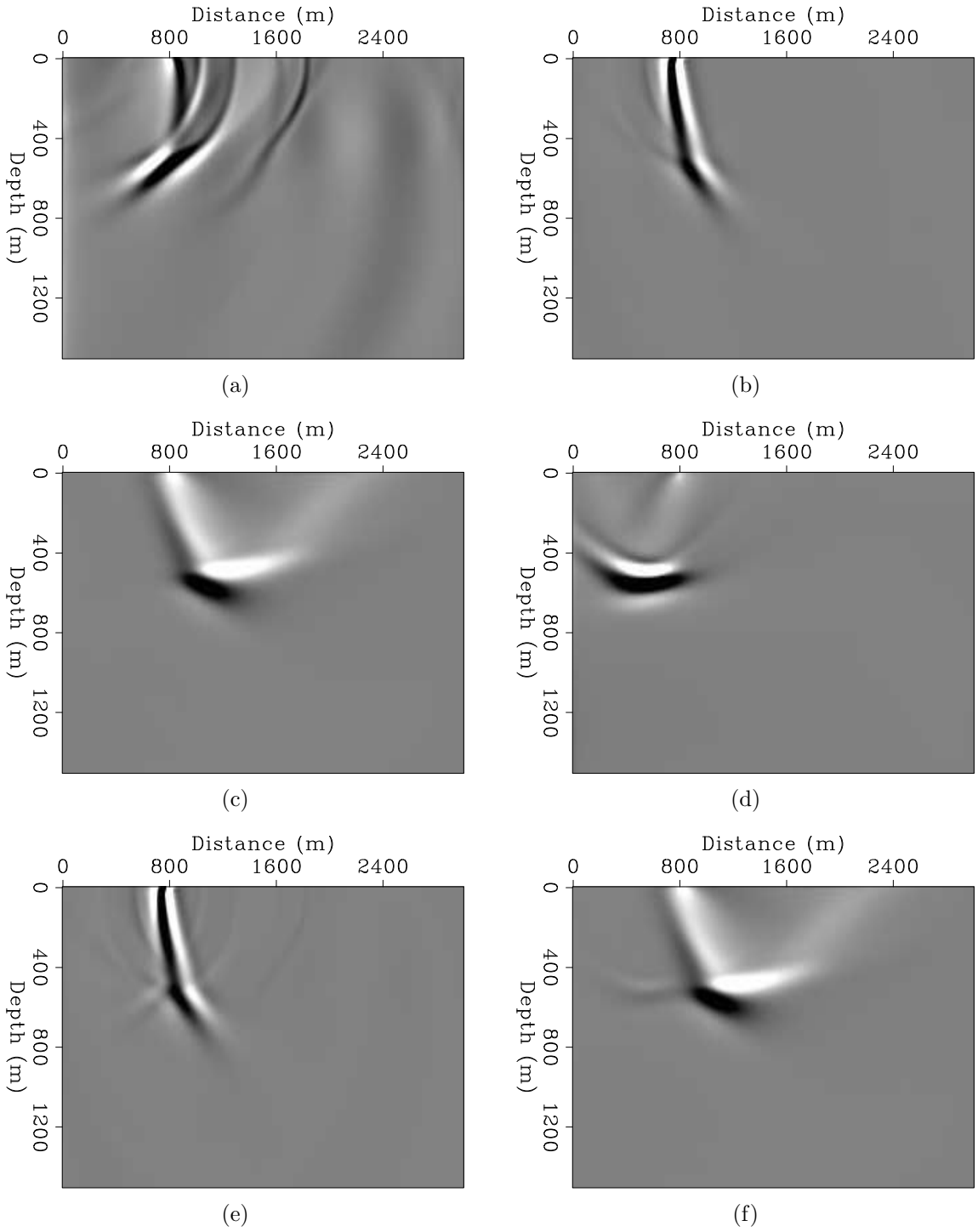

Figure 9: Different horizontally decomposed RTM images from the single shot profile in Figure 4(a) along with smooth migration velocity in Figure 5(a): (a) using the rightgoing source and leftgoing receiver wavefields, (b) using the leftgoing source and rightgoing receiver wavefields, (c) using the rightgoing source and rightgoing receiver wavefields, and (d) using the leftgoing source and leftgoing receiver wavefields. (e) The sum of the images (a) and (b) equivalent to Equation 9. (f) The sum of the images (c) and (d). [**ER**]

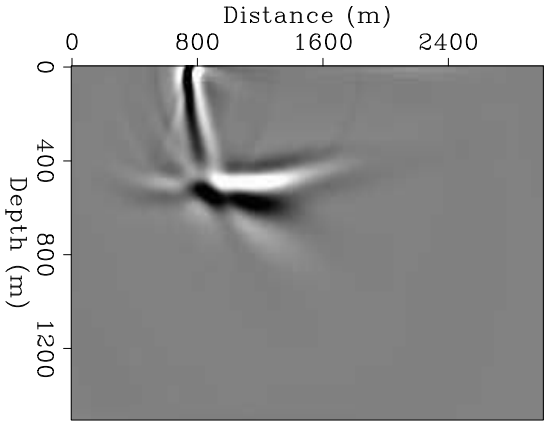

Figure 10: The RTM image from the Cartesian backscatter-based imaging condition as in Equation 10, i.e. the sum of Figure 8(e) and Figure 9(e). [**ER**]

attenuated using the low-cut filter.

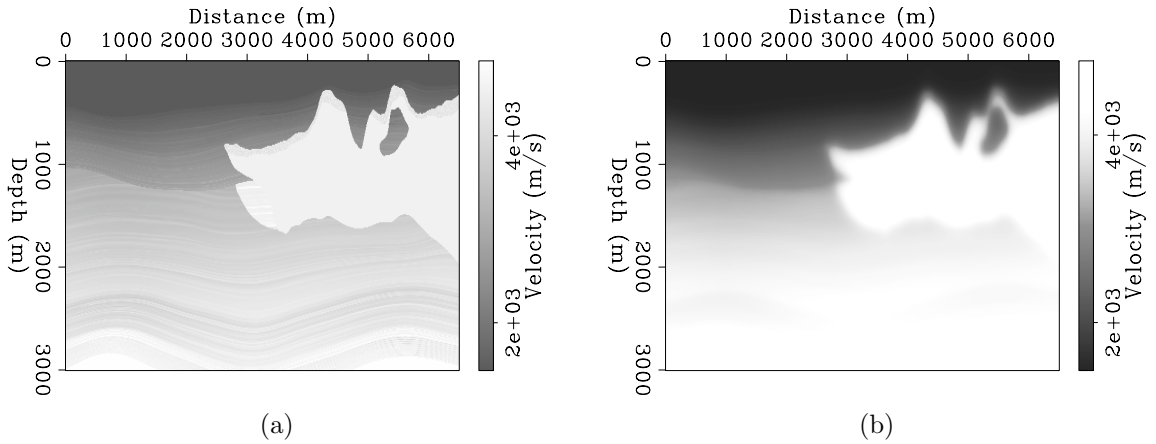

Figure 11: (a) A 2-D velocity model windowed from the SEAM model. (b) The smoothed velocity model used as the migration velocity. [**ER**]

Figures 13(a) to 13(d) illustrate the vertically decomposed RTM images corresponding to the four decomposed images on the right-hand side of Equation 7. Figure 13(b) results from the upgoing source and downgoing receiver wavefields. This figure contains artifacts at shallow depths which have the same origin as those in Figure 8(b).

Figure 13(e) illustrates the RTM images the vertical backscatter-based imaging condition. As shown in the figure, the illumination of steeply dipping reflectors is poor. In contrast, Figure 13(f) represents the decomposed images from the decomposed source and receiver wavefields that have been propagated in vertically opposite directions.

On the other hand, Figures 14(a) to 14(d) show the four different decomposed RTM images based on horizontal propagation directions of source and receiver wavefields. We can see that Figures 14(a) and 14(b) illustrate not only the images of steeply dipping reflectors but also artifacts in the shallow parts. These artifacts have

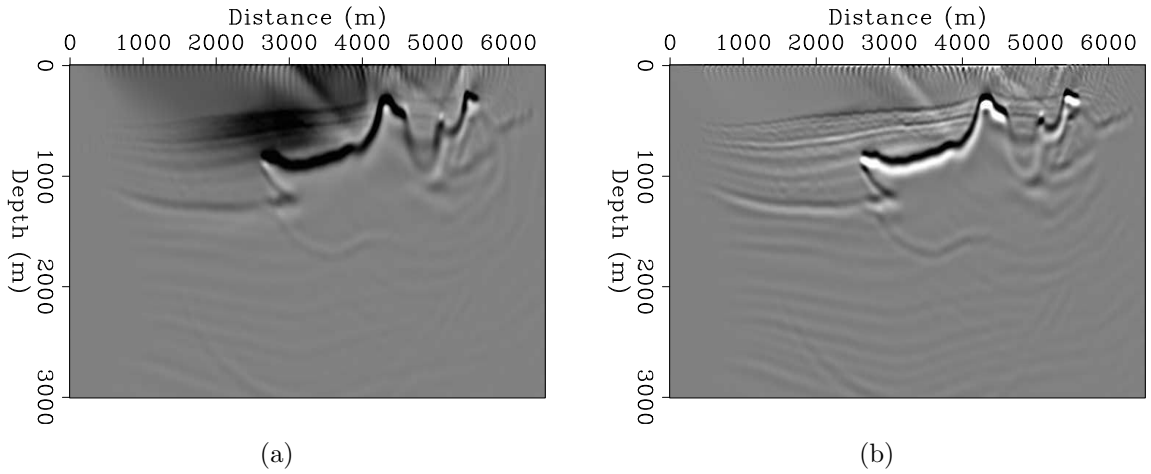

Figure 12: (a) A conventional RTM image of an entire 2-D synthetic data set using the cross-correlation imaging condition in Equation 1. (b) A causal low-cut filtered result of the image in (a). [**CR**]

the same origin as those in Figure 9(e).

Figure 14(e) is the result of using the imaging condition in Equation 9, i.e. the horizontal imaging condition. As shown in the figure, this imaging condition can image steeply dipping reflectors to an extent; however, most of low-angle reflectors cannot be imaged. In contrast, Figure 14(f), which involves the cross-correlation of the decomposed source and receiver wavefields caused by horizontally forward-scattered events, contains the major artifacts in the shallow parts of the model and the images of low-angle reflectors.

Figure 15 illustrates the result of using the Cartesian backscatter-based imaging condition, i.e. Equations 10. As shown in the figure, the result has the benefits of both vertical and horizontal imaging conditions. Both steeply dipping and low-angle reflectors are well imaged. In addition, Figure 15 contains artifacts in the shallow parts as a result of Figures 13(b), 14(a), and 14(b). However, strong RTM artifacts have significantly been attenuated.

It can be seen that the RTM image (Figure 15) using the Cartesian backscatter-based imaging condition, as in Equation 10, contains less strong artifacts compared to the conventional RTM image (Figure 12(a)) and the low-cut filtered RTM image (Figure 12(b)).

Thus, the combination of the vertical and horizontal imaging conditions is an effective technique for attenuating typical RTM artifacts, especially for complex velocity models. However, further investigation is necessary for removing the remaining artifacts in the shallow parts of the migrated images.

A possible solution is to modify the F-K filters in Equations 11 to 14, so there is no overlap between the decomposed wavefields with opposite propagation directions.

In this study, I also tried using fan filters to decompose wavefields in the F-K domain. These filters aimed to limit the aperture of propagation directions of wavefields. However, as a result of the FFT of discontinuous functions, there still remained the overlap between the decomposed wavefields with opposite propagation directions.

CONCLUSIONS

RTM can image steeply dipping reflectors and overturned events. However, the conventional correlation-based imaging condition in RTM always produces strong low-frequency artifacts. To suppress these artifacts, an imaging condition using appropriate decomposed source and receiver wavefields based on their propagation direction has been applied and examined. This imaging condition contains only the backward scattered events based on Cartesian directions. The imaging condition discussed in this paper successfully attenuates such artifacts in complex velocity models compared to applying a low-cut filter. However, there are still remaining artifacts in the decomposed RTM images. These are caused by the cross-correlation between the upgoing components of the direct source wavefields and the downgoing components of the backscattering of receiver wavefields. Thus, further investigation is still necessary to remove these residual artifacts.

ACKNOWLEDGMENTS

I would like to thank Biondo Biondi, Mandy Wong, Sjoerd de Ridder, Ali Almomin, and the other SEP colleagues for their valuable comments and suggestions. I also thank Exxon Mobil for providing the SEAM Phase 1 model used in this study.

REFERENCES

Almomin, A., B. Biondi, and R. Clapp, 2011, Combining forward-scattered and back-scattered wavefields in velocity analysis: SEP-Report, **143**, 77–84.

Baysal, E., D. D. Kosloff, and J. W. C. Sherwood, 1983, Reverse time migration: Geophysics, **48**, 1514–1524.

Biondi, B. L., 2005, 3-d seismic imaging: Stanford Exploration Project.

Cerjan, C., D. Kosloff, R. Kosloff, and M. Reshef, 1985, A nonreflecting boundary condition for discrete acoustic and elastic wave equations: Geophysics, **50**, 705–708.

Chattopadhyay, S. and G. A. McMechan, 2008, Imaging conditions for prestack reverse-time migration: Geophysics, **73**, S81–S89.

Claerbout, J. F., 1985, Imaging the earth's interior: Blackwell Science Inc.

Clayton, R. W. and B. Engquist, 1980, Absorbing boundary conditions for wave-equation migration: Geophysics, **45**, 895–904.

Dablain, M. A., 1986, The application of high-order differencing to the scalar wave equation: Geophysics, **51**, 54–66.

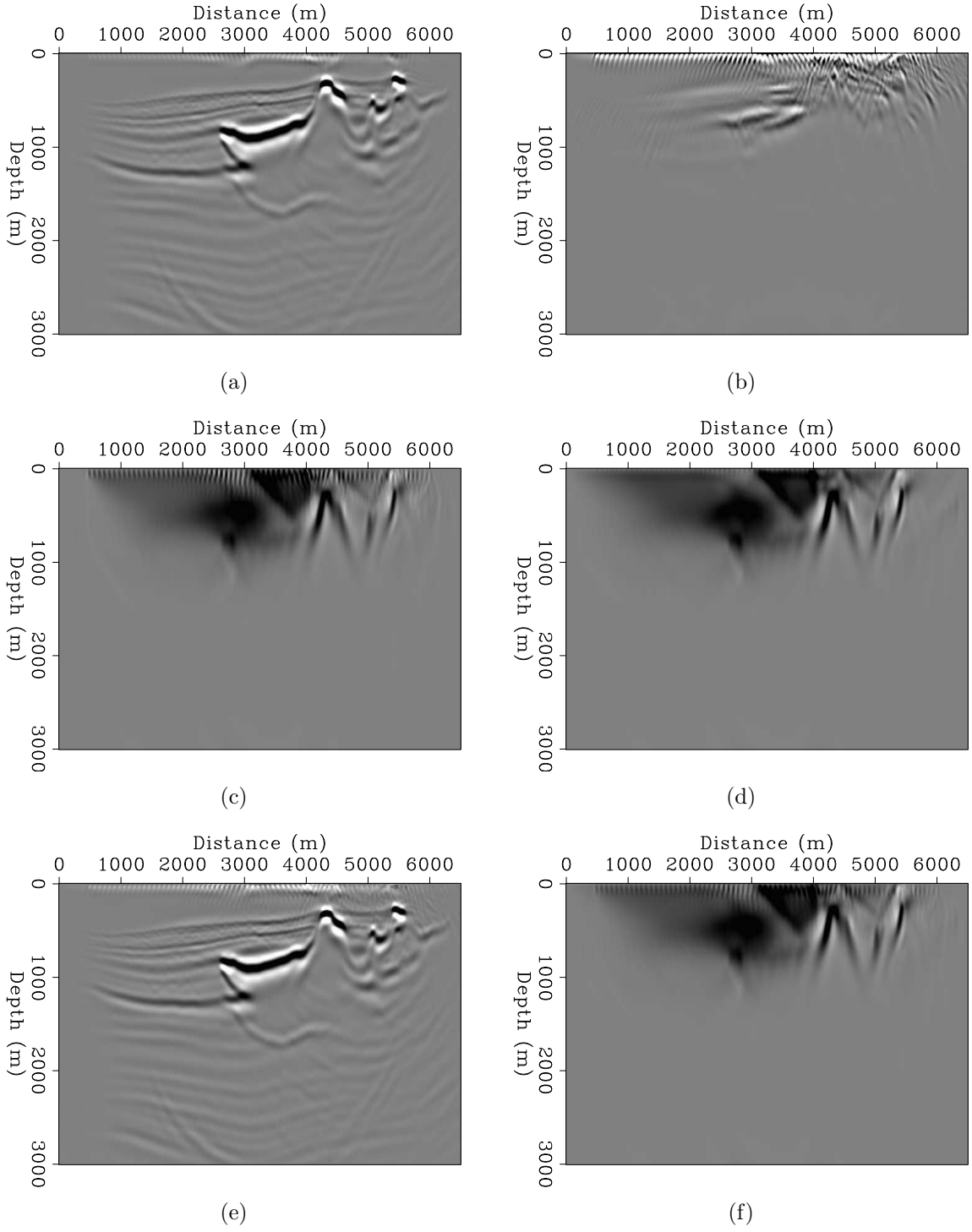

Figure 13: Different vertically decomposed RTM images from 2-D synthetic data along with the smoothed migration velocity in Figure 11(b): (a) using the downgoing source and upgoing receiver wavefields, (b) using the upgoing source and downgoing receiver wavefields, (c) using the downgoing source and downgoing receiver wavefields, and (d) using the upgoing source and upgoing receiver wavefields. (e) The sum of the images (a) and (b) equivalent to Equation 8. (f) The sum of the images (c) and (d). [**CR**]

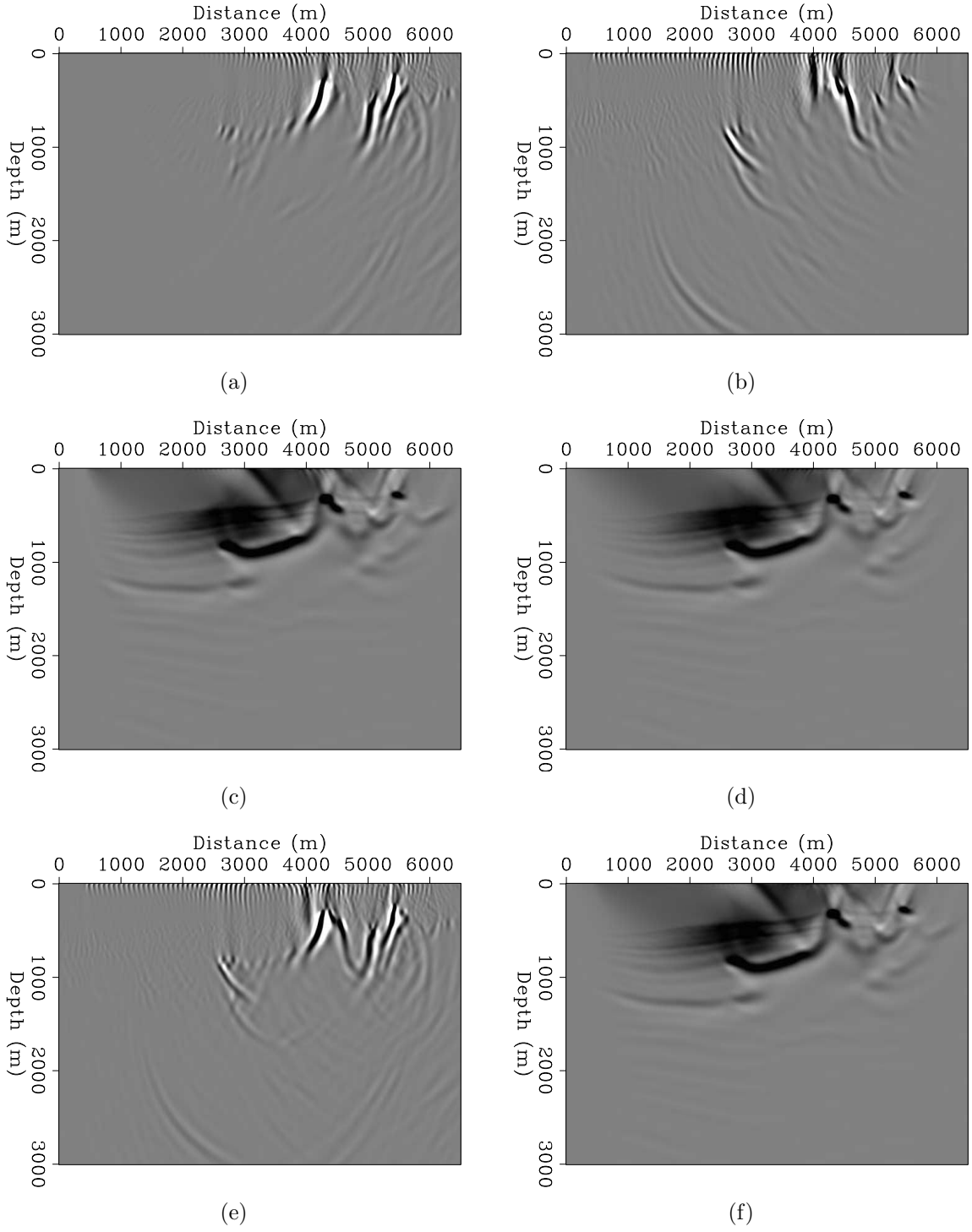

Figure 14: Different horizontally decomposed RTM images from 2-D synthetic data along with the smoothed migration velocity in Figure 11(b): (a) using the rightgoing source and leftgoing receiver wavefields, (b) using the leftgoing source and rightgoing receiver wavefields, (c) using the rightgoing source and rightgoing receiver wavefields, and (d) using the leftgoing source and leftgoing receiver wavefields. (e) The sum of the images (a) and (b) equivalent to Equation 9. (f) The sum of the images (c) and (d). [**CR**]

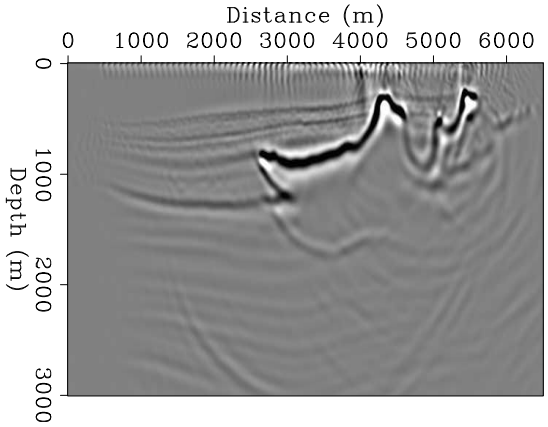

Figure 15: The RTM image from the Cartesian backscatter-based imaging condition as in Equation 10, i.e. the sum of Figure 13(e) and Figure 14(e). [**CR**]

Etgen, J., S. H. Gray, and Y. Zhang, 2009, An overview of depth imaging in exploration geophysics: Geophysics, **74**, WCA5–WCA17.

Fei, T. W., Y. Luo, S. Aramco, and G. T. Schuster, 2010, De-blending reverse-time migration: SEG Technical Program Expanded Abstracts, **29**, 3130–3134.

Fletcher, R. F., P. Fowler, P. Kitchenside, and U. Albertin, 2006, Suppressing unwanted internal reflections in prestack reverse-time migration: Geophysics, **71**, E79–E82.

Guitton, A., B. Kaelin, and B. Biondi, 2006, Least-square attenuation of reverse-time migration artifacts: SEG Technical Program Expanded Abstracts, **25**, 2348–2352.

Hu, L.-Z. and G. A. McMechan, 1987, Wave-field transformations of vertical seismic profiles: Geophysics, **52**, 307–321.

Liu, F., G. Zhang, S. A. Morton, and J. P. Leveille, 2007, Reverse-time migration using one-way wavefield imaging condition: SEG Technical Program Expanded Abstracts, **26**, 2170–2174.

———, 2011, An effective imaging condition for reverse-time migration using wavefield decomposition: Geophysics, **76**, S29–S39.

Robein, E., 2010, Seismic imaging: A review of the techniques, their principles, merits and limitations: EAGE.

Suh, S. Y. and J. Cai, 2009, Reverse-time migration by fan filtering plus wavefield decomposition: SEG Technical Program Expanded Abstracts, **28**, 2804–2808.

Valenciano, A. A. and B. Biondi, 2003, 2-d deconvolution imaging condition for shot-profile migration: SEG Technical Program Expanded Abstracts, **22**, 1059–1062.

Whitmore, N. D., 1983, Iterative depth migration by backward time propagation: SEG Technical Program Expanded Abstracts, **2**, 382–385.

Xie, X.-B. and R.-S. Wu, 2006, A depth migration method based on the full-wave reverse-time calculation and local one-way propagation: SEG Technical Program Expanded Abstracts, **25**, 2333–2337.

Yoon, K. and K. J. Marfurt, 2006, Reverse-time migration using the poynting vector: Exploration Geophysics, **37**, 102–107.

Yoon, K., K. J. Marfurt, and W. Starr, 2004, Challenges in reverse-time migration: SEG Technical Program Expanded Abstracts, **23**, 1057–1060.

Zhang, Y. and J. Sun, 2009, Practical issues in reverse time migration: True amplitude

gathers, noise removal and harmonic source encoding: First Break, **27**, 53–59.